Appl. Phys. A 75, 101–112 (2002) / Digital Object Identifier (DOI) 10.1007/s003390101059

Applied Physics A
Materials
Science & Processing

Defects in III–V semiconductor surfaces

Ph. Ebert*

Institut für Festkörperforschung, Forschungszentrum Jülich GmbH, 52 425 Jülich, Germany

Received: 10 May 2001/Accepted: 23 July 2001/Published online: 3 April 2002 – © Springer-Verlag 2002

Abstract. This work reports the measurement of the nano-scale physical properties of surface vacancies and the extraction of the types and concentrations of dopant atoms and point defects inside compound semiconductors, primarily by cross-sectional scanning tunneling microscopy on cleavage surfaces of III–V semiconductors. The results provide the basis to determine the physical mechanisms governing the interactions, the formation, the electronic properties, and the compensation effects of surface as well as bulk point defects and dopant atoms.

PACS: 71.55.Eq; 73.20.Hb; 68.37.Ef

The electrical properties of semiconductors and thus their applicability in electronic devices are to a large degree governed by defects and dopant atoms incorporated during growth and production processes. Although some defects and dopant atoms may be desired to achieve the optimum device properties, other defects may be formed unintentionally and counteract the desired electronic properties. Therefore, considerable research efforts were focussed on determining the nano-scale physics governing the formation of point defects, the incorporation behavior of impurities, and their respective electronic properties.

Unfortunately, a direct experimental access to point defects in semiconductors is very difficult, because most experimental techniques rely on the interpretation of macroscopic data of differently processed crystals or on signals integrated over a large set of usually unknown defects. Conclusions about point defects on the *atomic level* were necessarily limited. In contrast, cross-sectional scanning tunneling microscopy (STM) allows us to directly image with atomic resolution *individual* point defects and dopant atoms. Cross-sectional scanning tunneling microscopy is based on a simple concept: the defects inside the crystal are exposed by *cleavage* on a surface and subsequently imaged with atomic resolution using STM. Such images yielded a large variety of atomically resolved data about point defects and dopant atoms. The results provided not only significant progress in the understanding of the fundamental physics of point defects in compound semiconductor surfaces, but it has even been possible to draw conclusions about properties of defects inside semiconductor crystals and the physics governing these bulk point defects [1].

The present paper illustrates using selected examples of the progress we achieved in recent years in determining the physics governing the nano-scale properties of point defects in compound semiconductors and their surfaces. We concentrate, on the one hand, on anion surface vacancies as the purest example for *surface* defects in cleavage surfaces of III–V semiconductors and demonstrate the determination of the surface vacancies' key properties, such as charge-transition levels, electrical charge states, lattice relaxation, and interactions. On the other hand, it is shown how to extract the physics governing *bulk* point defects by STM. Particular focus will be on the compensation and incorporation behavior of dopant atoms in bulk GaAs and the influence of electrical charges.

1 Surface vacancies in (110) cleavage surfaces of III–V semiconductors

Figure 1 shows a large-scale scanning tunneling microscope image of a typical (110) cleavage surface of a *p*-doped InP crystal. The image shows the periodic structure of the clean cleavage surface and a number of defects and dopant atoms. Such images contain detailed information about the *types and properties* of the defects and dopant atoms. However, before addressing those in detail, we have first to briefly recall the structure of the defect-free surface, in order to interpret the STM image properly.

Zincblende-structure III–V compound semiconductors cleave along their non-polar (110) planes, yielding surfaces which are similar to an ideal truncated bulk (110) plane, i.e. a 1×1 unit cell with one anion (group-V element, P, As, etc.) and one cation (group-III element, In, Ga, etc.) each having a broken bond. This unrelaxed structure is, however, unstable and the surface lowers its energy by slightly displacing

*(Fax: +49-2461/61-6444, E-mail: p.ebert@fz-juelich.de)

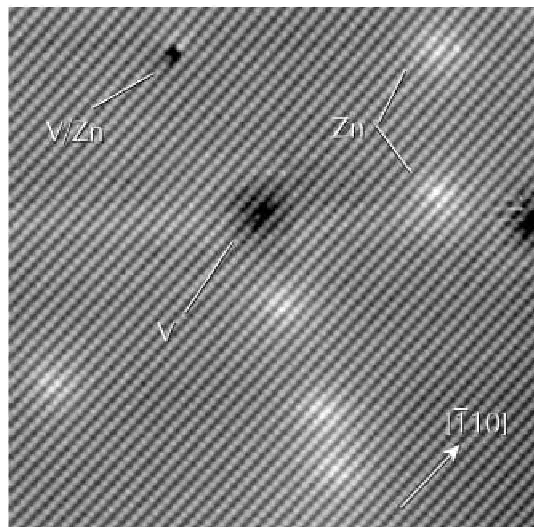

Fig. 1. Overview of defects on InP (110) surfaces. In addition to phosphorus vacancies appearing as black depressions, white elevations surounding Zn L-dopant atoms can be observed (sample voltage -2.2 V). Adapted with permission from [51]. ©1996 American Physical Society

the surface anions outward relative to the surface cations, while the bond lengths remain essentially unchanged. The relaxation is mostly a pure bond-rotation relaxation [2, 3] and results in a buckling of the surface anion–cation bond by $29 \pm 3°$ independent of the semiconductor material [4–6]. It has been suggested that the preferred planar threefold coordination with occupied sp^2-like and empty p_z-like orbitals at the group-III atoms and the three-dimensional (incomplete) tetrahedral coordination with sp^3-like orbitals at the group-V atoms are the driving forces of the relaxation [6–9].

The relaxation pushes the surface states associated with the broken bonds out of the fundamental band gap, leading to one fully occupied and one completely empty surface state in the valence and conduction bands, respectively [10, 11]. These states are localized above the anions (filled surface state) and cations (empty surface state), respectively. Therefore, STM images measured at negative sample voltages show the occupied dangling bonds above the anions, whereas the empty dangling bonds above the cations are visible in STM images acquired at positive sample voltages [12]. Note that no surface states exist in the fundamental band gap and thus the (110) surfaces of most III–V semiconductors are not pinned [13–19]. The Fermi energy at the defect-free surface is controlled by the doping of the crystal. Only defects can introduce gap states and pin the Fermi energy at the surface. The basic picture of two dangling bond states is slightly modified due to additional surface resonances lying deeper in the bands and affecting the fine structure of STM images at larger tunneling voltages [20]. For the present purpose it is, however, sufficient to consider the dangling bond states only. Note that this particular unpinned surface structure is essential for the successful application of cross-sectional scanning tunneling microscopy to bulk defects.

On the basis of the above-mentioned surface structure it is evident that Fig. 1 shows the occupied dangling bonds localized at the phosphorus atoms in the InP (110) surface. In addition, three types of defects and dopant atoms occur. The localized white contrast features marked 'Zn' are Zn-dopant atoms. These are *bulk* impurities incorporated during growth of the InP crystal. We will address them in Sect. 2. The wide dark contrast features marked 'V' are individual phosphorus *surface* vacancies, whereas the localized dark contrast features marked 'V/Zn' are vacancy–dopant complexes. Both latter defects are purely *surface defects* not present in the bulk of this crystal and formed after cleavage on the surface. In fact vacancies are the purest example of surface defects on III–V semiconductor cleavage surfaces. They spontaneously form and have a large variety of very intriguing properties described in this section.

1.1 Observation of surface vacancies with atomic resolution

Vacancies were observed on almost all cleavage surfaces of III–V semiconductors. Up to date, As vacancies have been reported in GaAs [21–23] and InAs [24], P vacancies in InP [25–27] and GaP [26, 28], Sb vacancies in InSb [29, 30], and Ga vacancies in GaAs [22, 31, 32] and GaP [33] (110) surfaces. Recently, vacancies have also been observed in CdSe and CdS cleavage surfaces [34]. All vacancies have similar properties. Here we concentrate on the phosphorus vacancies in InP(110) surfaces as a model system since the most comprehensive understanding has been reached for this particular system. A full overview of all vacancies can be found in [1].

Figure 2 shows high-resolution STM images of the occupied- and empty-state images of two phosphorus vacancies on *p*-doped InP(110). The main feature of these vacancies as well as of all other vacancies is that the anion vacancies give rise to one localized hole or missing occupied dangling bond but no missing empty state. Cation vacancies exhibit one missing empty dangling bond but no missing occupied states. The missing state is due to the missing atom to which the dangling bond has been connected. This particular pattern is a fingerprint of the vacancies. This fingerprint is now corroborated by simulations [35–37], much more detailed experimental data, showing for example the formation of the vacancies [38], and combined theoretical and experimental works [33, 37, 39].

1.2 The electronic structure of vacancies

1.2.1 The electrical charge. Vacancies give rise in the constant-current STM images to a contrast consisting of two

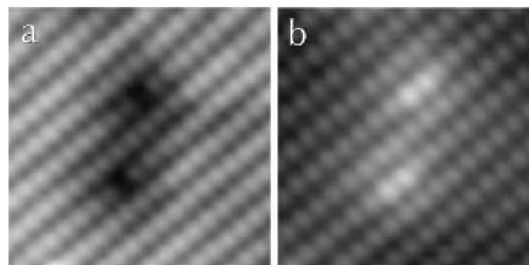

Fig. 2a,b. Scanning tunneling microscope images of the **a** occupied density of states measured at -2.9 V and **b** empty density of states acquired at $+2$ V sample voltage of two phosphorus vacancies in the *p*-doped InP (110) surface

fundamentally different parts. The first part is a small "hole" mentioned as the fingerprint above, which has a lateral dimension of one dangling bond state and arises from the missing atom. The second part is illustrated in Fig. 3, which shows four constant-current STM images of several P vacancies in the p-doped InP(110) surface obtained at different negative tunneling voltages. The vacancies are surrounded by a long-range depression, whose magnitude increases with decreasing magnitude of the voltage (Fig. 3a–d). In Fig. 3a, at a high negative tunneling voltage, the defects are imaged as small, up to 0.07 nm deep depressions. At low voltages the depression reaches a diameter of typically 4 to 5 nm.

The voltage-dependent long-range depression surrounding the P vacancies is the signature of a positive charge localized at the vacancies [28, 40, 41]: a positive charge induces a local downward band bending which reduces the number of occupied states near the valence-band maximum, contributing to the tunnel current. This results in a local decrease of the tunnel current, and the electronic feedback loop of the STM responds to this by reducing the tip-to-sample distance in order to keep the current constant (yielding a depression in the image). At low magnitudes of negative tunneling voltages a large fraction of states cannot contribute to the current due to the band bending. This leads to a deep and wide depression (Fig. 3d). With increasing magnitude of negative tunneling voltage, more surface states within a larger interval of energy in the valence band contribute to the tunnel current. Thus, the fraction of states inhibited from participating in the tunnel process by the local band bending decreases and, consequently, only the small and narrow depression induced by the missing atoms is observed (Fig. 3a). Such voltage-dependent elevations and depressions in STM images are the signature of localized electrical charges, which allow a determination of the polarity [42] and the magnitude of the charge [43]. A detailed discussion of the quantitative charge determination

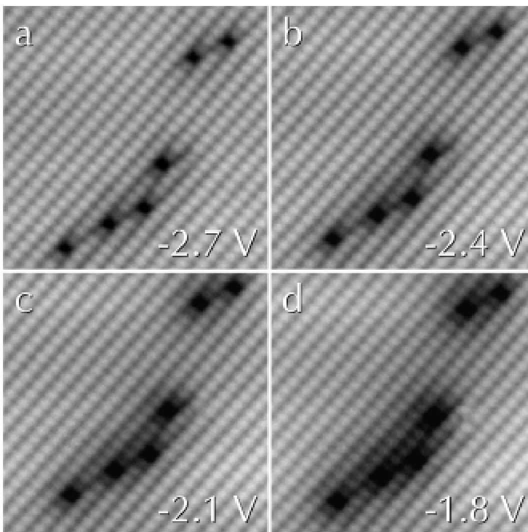

Fig. 3. High-resolution constant-current images of the occupied states of a group of P vacancies on InP (110) obtained at different sample voltages indicated in the lower right corner of each frame. The defects consist of single missing occupied dangling bonds and are surrounded by long range voltage-dependent dark-contrast areas. The long range depressions are the signature of a local downward band bending induced by the positive charge of vacancies. Adapted with permission from [38]. ©1995 American Physical Society

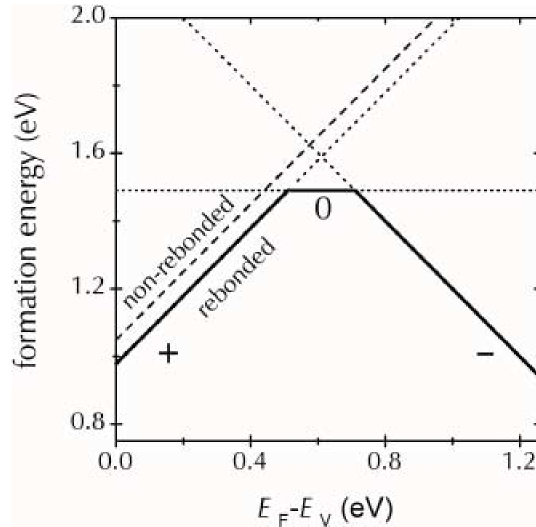

Fig. 4. Calculated formation energies for differently charged P vacancies on InP (110) surfaces under phosphorus rich conditions versus Fermi energy E_F (0 eV: valence band maximum). On p-doped surfaces a single positively charged P vacancy is stable, whereas a single negatively charged P vacancy has the lowest energy on n-doped surfaces. Adapted from [44]. (courtesy of G. Schwarz)

of defects is given in [1]. In the present case of a p-doped InP (110) surface the dark contrast is due to a $+1e$ charge of the P vacancy and the white contrast indicates a $-1e$ charge of the Zn-dopant atom. On n-doped InP (110) surfaces we found that P vacancies are negatively charged [26].

At this stage we compare our results of the electrical charges with calculations. We consider here only the most recent state of the art calculations of anion vacancies in the (110) surfaces, because earlier ones did not include the lattice relaxations and/or their results are not consistent. Figure 4 shows the formation energy for P vacancies in InP (110) surfaces [44]. Similar results were obtained for As vacancies in GaAs(110) [35, 36, 44, 45] and P vacancies in GaP(110) [44, 46]. These calculations predict for all anion vacancies a single positive charge in p-doped and a single negative charge in n-doped surfaces, independent of the material, in agreement with the experimental data of anion vacancies not only in InP but also in GaAs [43, 47–49], InP [50, 51], and GaP [26] (110) surfaces. Thus there is a *qualitative* agreement between theory and experiment.

1.2.2 Charge-transition levels. The observation of different charge states of vacancies on n- and p-doped surfaces is a direct consequence of localized defect states introduced in the band gap by the vacancies. These gap states are crucial for the understanding of the effect of vacancies on the materials' properties. Therefore there have been a number of attempts to determine the exact energy of these localized defect states. The data exhibited, however, large discrepancies: scanning tunneling spectroscopy measurements yielded a local downward band bending of 0.1 eV for positively charged As vacancies in p-doped GaAs(110) [23], whereas surface photovoltage measurements found a band bending of 0.53 ± 0.03 eV [52] at the site of the As vacancy. Similarly, the results for calculated energy levels deviate: density functional theory (DFT) calculations predicted the charge-transition level (+/0) to be 0.32 eV [35] and 0.1 eV [36], and

the lowest Kohn–Sham eigenvalues in the band gap to be 0.73 eV [35] and 0.06 eV [36] above the valence-band maximum. Discrepancies such as those pointed out above can arise due to limitations of the methods used. In particular the quantities measured are in most cases not comparable since the experimental conditions, notably the concentration of the vacancies, are by far not the same in all experiments leading to widely scattered band-bending values. Finally, the quantities discussed to describe the position of the defect level, i.e. Kohn–Sham eigenvalues within DFT, band bending, and charge-transition levels (also known as charge-transfer levels), are *different physical quantities* and thus (typically) deviate from each other significantly. Therefore, we concentrated on determining the energy position of the charge-transition levels, since those can be measured reliably *and* calculated well. At a first stage, the approximate positions of the charge-transition levels are deduced from the observed charges of the vacancies. Second, the exact determination of the energy of the charge-transition levels in the band gap is shown.

If a vacancy has an electronic energy level in the band gap, the charge of the vacancy may be influenced by the doping of the crystal. The defect state can be either filled or empty, depending on the relative position of the Fermi energy with respect to the charge-transition level: if the Fermi energy lies below the charge-transition level the defect has one electron less than if the Fermi energy is above it. On the basis of the observed charges of the P vacancies, it can thus be concluded that the $(+/0)$ and $(0/-)$ charge-transition levels are in the band gap. The $(2+/+)$ charge-transition level must be below the valence-band maximum. This result agrees with the most recent theoretical calculations [35, 36, 44–46] and with the data in Fig. 4.

At this stage the information about the energy of charge-transition levels is limited to the knowledge of whether charge-transition levels are in the band gap or not. We also extracted *quantitative* values of the energy of charge-transition levels in the band gap by measuring the concentration of the vacancies as a function of the band bending [39]. The concentration of P vacancies was varied by annealing initially defect-free p-doped InP(110) cleavage surfaces at 435 K (see Sect. 1.4) [38]. Figure 5 shows the band bending (filled diamonds, left axis) and the vacancy concentration (open circles, right axis) as a function of the annealing time. During heat treatment the vacancy concentration increases with increasing annealing time. Similarly, the position of the Fermi level, which on well-cleaved defect-free surfaces is close to the top of the valence-band maximum for p-type samples, is found to shift toward mid-gap upon annealing, as measured by photoelectron spectroscopy (PES). The band bending reaches a saturation value of 0.65 eV at vacancy concentrations of $5 \times 10^{12}\,\mathrm{cm}^{-2}$ [39]. Figure 5 also demonstrates that the Fermi-level shift is directly correlated to the increase of the vacancy concentration.

The energy of the charge-transition level in the band gap E_{sd} can now be extracted as follows. The charge per unit surface area in the surface layer Q_{ss} is exactly compensated by the charge density per unit surface area in the depletion layer Q_{sc} [14]. The charge per unit surface area induced by a concentration n_{sd} of $+1e$-charged P surface vacancies is [14]

$$Q_{\mathrm{ss}} = \frac{e \cdot n_{\mathrm{sd}}}{\exp((E_{\mathrm{F}} - E_{\mathrm{sd}})/kT) + 1} \qquad (1)$$

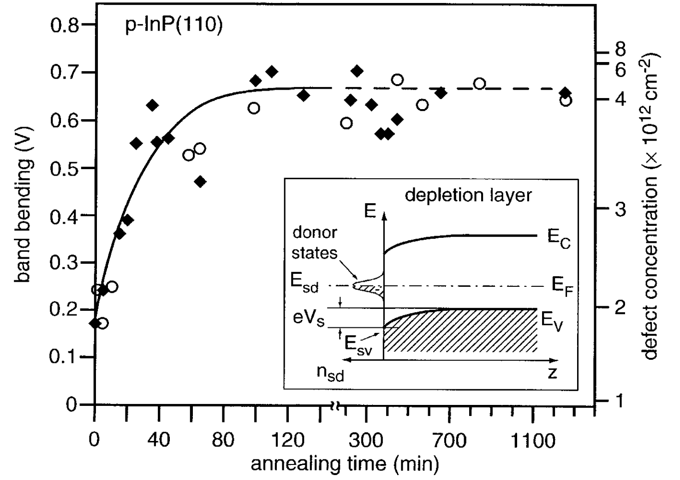

Fig. 5. The band bending (*filled diamonds*, *left axis*) and the vacancy concentration (*empty circles*, *right axis*) on the InP(110) surface as a function of the annealing time at 435 K. The *solid line* is the vacancy concentration calculated on basis of Eqs. (1) and (2) and a fit through the measured band bending values. The *dashed line* shows the saturation value. The *right scale* is chosen such that according to Eqs. (1) and (2) the vacancy concentration is shown on a scale linear proportional to the band bending. The *inset* shows a schematic drawing of the depletion region in case of a fully pinned surface. Reprinted with permission from [39]. ©2000 American Physical Society

where E_{F} is the Fermi energy. The difference in energies of the charge-transition level and the Fermi level $E_{\mathrm{sd}} - E_{\mathrm{F}}$ is given by $(E_{\mathrm{sd}} - E_{\mathrm{sv}}) - (E_{\mathrm{v}} - E_{\mathrm{sv}}) - (E_{\mathrm{F}} - E_{\mathrm{v}})$ (for definitions see inset in Fig. 5; E_{v} and E_{sv} are the positions of the valence band in the bulk and at the surface, respectively), where $E_{\mathrm{v}} - E_{\mathrm{sv}}$ is the band bending eV_s measured by photoelectron spectroscopy at the surface. The charge density per unit surface area in the depletion layer Q_{sc} compensating Q_{ss} is

$$Q_{\mathrm{sc}} = \sqrt{2\varepsilon_{\mathrm{r}}\varepsilon_0 \cdot n \cdot kT \cdot (\exp(-eV_{\mathrm{s}}/kT) + (eV_{\mathrm{s}}/kT) - 1)} \qquad (2)$$

where n is the concentration of charge carriers introduced by the dopant atoms. The energy difference between the Fermi energy and the valence-band maximum in the bulk has been determined for a non-degenerate InP crystal from the carrier concentration of $(1.3 - 2.1) \cdot 10^{18}\,\mathrm{cm}^{-3}$.

Equations (1) and (2) permit a determination of the energy of the charge-transfer level E_{sd} using the vacancy-concentration dependence of the band bending of Fig. 5. The $(+/0)$ charge-transition level of the P vacancy was found to be (0.75 ± 0.1) eV above the valence-band maximum at room temperature [39]. Note that the knowledge of the defect concentrations is crucial to determine the energy of the charge-transition level from a measurement of the band bending.

Recent calculations for P vacancies in InP(110) surfaces yield a $(+/0)$ charge-transition level of 0.52 eV above the valence-band maximum [39, 44], in agreement with the experimental value taking the accuracy of the calculation (band-gap underestimation, supercell, cutoff, etc.) into account.

1.3 The geometric structure of vacancies

The energies of the defect levels and in particular of the charge-transition levels are closely related to the atomic structure of the vacancy. Figure 4 shows the formation energies for

two different vacancy structures, a symmetric non-rebonded one and a non-symmetric rebonded one. Before addressing these two structures in more detail it is necessary to recall that the determination of the geometric structure of a vacancy turned out to be a very complicated task. First, most calculated relaxations vary considerably from calculation to calculation [23, 35–37, 45], because the energy differences between competing structures are small. Secondly, experiments [23, 26] were interpreted in most cases wrongly, since it is not possible to correlate directly maxima of the density of states with atomic positions [35, 36]. In view of this situation the structure has been a hotly debated topic [23, 35–37, 45, 53, 54]. An unambiguous structure determination, clarifying the situation, is nevertheless possible [39].

In order to differentiate between different vacancy configurations we have first to address the two lowest-energy structures. All most recent density functional theory calculations predict an inward relaxation of the neighboring atoms of the positively charged anion vacancies. However, the details deviate: Kim and Chelikowsky [36, 45] found that the three *non-rebonded* neighboring Ga atoms of the $+1e$-charged As vacancy relax *symmetrically* inward with respect to the $(1\bar{1}0)$ mirror plane. Zhang and Zunger [35] found, however, that a *non-symmetric rebonded* structure reduces the total energy by an additional 0.16 eV for the $+1e$-charged As vacancy. The situation is similar for the $+1e$-charged P vacancies on InP (110) studied here [44], except that the energy difference between the two structures is even smaller (about 0.08 meV). Thus, the $+1e$-charged P vacancies on InP (110) can have two configurations, a symmetric and a non-symmetric structure, which are *almost degenerate* in energy.

The two structures can be distinguished by comparing simulated local density of states images with measured STM images [39]: Fig. 6a and b show the occupied (upper frames) and empty (lower frames) local density of states images calculated for (a1) and (a2) the non-symmetric vacancy structure and (b1) and (b2) for the symmetric vacancy configuration. Both vacancy configurations lead to clearly distinguishable STM images: the non-symmetric vacancy exhibits a pronounced asymmetry (Fig. 6a), whereas the symmetric vacancy shows a $(1\bar{1}0)$ mirror plane (Fig. 6b). However, both static structures are in conflict with the experimental STM images (Fig. 6d). The symmetric density of states in the STM images (Fig. 6d) disagrees with the non-symmetric vacancy configuration in Fig. 6a, while the empty-state STM images do not show any reduced separation of the two neighboring empty dangling bonds as predicted for the symmetric vacancy structure (Fig. 6 (b2)). Thus none of the *static* equilibrium vacancy configurations can be matched to the experimental observation.

This apparent conflict disappears, however, if one considers the nearly degenerate energies. In fact the barrier between the two structures is only 0.08 eV [39]. The low value of the barrier implies that, at room temperature, the vacancy flips between the two energetically more favorable non-symmetric configurations at a rate significantly higher than the time resolution of the STM. This concept of a thermally activated flip motion is in analogy to that of buckled dimers at the Si (001) surface [55, 56]. Figure 6c shows the local density of states assuming that the vacancy flips such that the STM probes the average of the two mirror configurations. The images agree very well with the experiment. In particular two major features, the nearly unchanged separation of the neighboring empty dangling bonds (Fig. 6 (c2)) and the depression of the neighboring occupied dangling bonds (Fig. 6 (c1)), are well reproduced. Thus the positively charged P vacancy in InP (110) surfaces is *non-symmetrically rebonded* and thermally flips between its two mirror structures at room temperature. Note that most problems with prior interpretation of the STM data and calculations arose from the fact that implicitly static conditions were assumed.

1.4 The thermal formation of vacancies

The flip motion is not the only dynamic property of vacancies. The presence of vacancies has long been assumed to be solely cleavage-induced [23, 25, 28, 30]. However, the major reason for the presence of monovacancies on cleavage surfaces is a low-temperature Langmuir desorption of atoms after cleavage of the crystals even at room temperature [38]. This mechanism was first demonstrated for P vacancies in *p*-doped InP (110) [38] and later confirmed to occur also on *p*- and *n*-doped GaAs (110) surfaces, where As and Ga vacancies are formed, respectively [57, 58]. Note that the temperature range of interest for the formation of monovacancies is considerably lower than that of the conventional Langmuir evaporation, where desorption occurs in the case of InP above

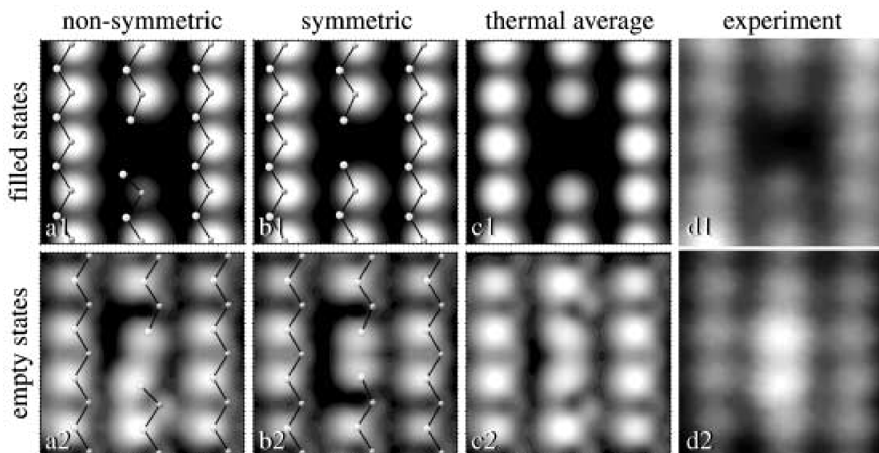

Fig. 6a–d. Simulated STM images deduced from the calculated local density of states 0.3 nm above the surface of $a+1e$ charged P vacancy on InP (110) surfaces for different atomic configurations **a**–**c** and experimental high resolution STM images of a P vacancy measured at **d1** -2.9 and **d2** $+2.0$ V. The simulation shows the occupied (upper frames, energy range from VBM to VBM-1 eV) and empty (lower frames, energy range from VBM to VBM $+2$ eV) states for **a1**, **a2** a non-symmetric rebonded, **b1**, **b2** a symmetric non-rebonded, **c1**, **c2** the thermal average of the non-symmetric rebonded vacancy configuration. The respective atomic configurations are superposed on the simulated images. Reprinted with permission from [39]. ©2000 American Physical Society

575 K and leads eventually to a decomposition of the material [59–62]. In our case the formation of vacancies starts at temperatures as low as room temperature.

Figure 7a to d show that with increasing annealing time in ultrahigh vacuum the concentration of the P monovacancies in p-doped InP (110) surfaces increases considerably. A similar increase of the vacancy concentration with time is observed for all temperatures studied (Fig. 7e). We achieved a maximum vacancy concentration of $5 \times 10^{12}\,\mathrm{cm}^{-2}$ after annealing the samples for about 500 min at 435 K. Actually at higher temperatures the vacancy concentrations (and the initial slope, $\mathrm{d}c_\mathrm{V}/\mathrm{d}t|_{t=0}$, as well as the maximum concentration) are lower again.

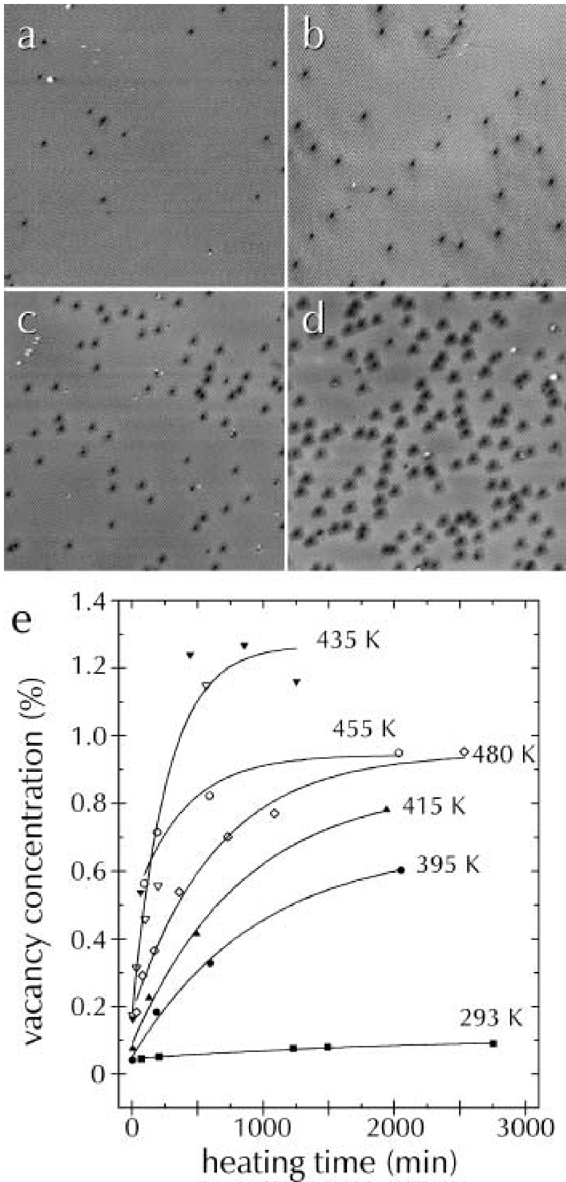

Fig. 7a–e. STM images showing the formation of P monovacancies on a p-doped InP (110) surface after heat treatment at 415 K for **a** 5, **b** 130, **c** 490, and **d** 1940 min. Each image shows an area of $70 \times 70\,\mathrm{nm}^2$. Reprinted with permission from [27]. ©1995 American Vacuum Sovciety and American Institute of Physics. **e** Vacancy concentration of the vacancies is displayed as a fraction of the P sublattice sites of the surface layer. The *solid lines* serve for guidance of the eye. Adapted with permission from [38]. ©1995 American Physical Society

Figure 8a shows the vacancy concentration as a function of the time after cleavage for three InP (110) surfaces with different carrier concentrations. Again, the concentration of the vacancies increases for each sample with time as for the higher temperatures shown in Fig. 7e. However, the rate of formation of the vacancies (slope of the data) as well as the concentration at constant time increases with increasing carrier concentration of the samples.

At this stage we discuss the results. First the data clearly demonstrates that the vacancy formation is thermal and not tip-induced [28, 63]. Second, in order to analyze the data, we

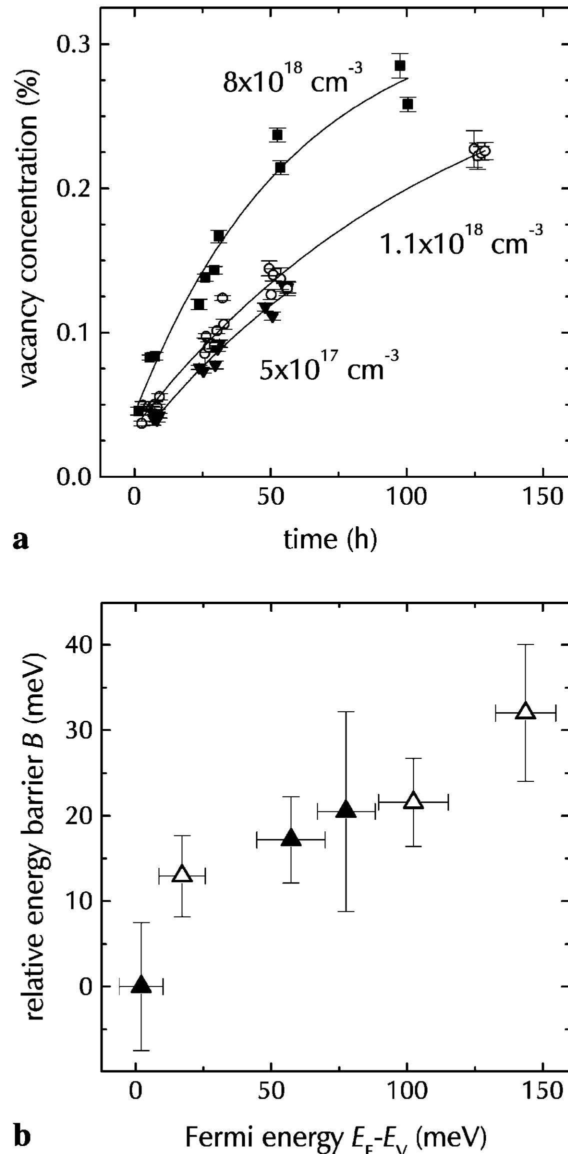

Fig. 8. a Concentrations of phosphorus vacancies in fraction of phosphorus surface lattice sites as a function of time after cleavage at room temperature. Shown are the data sets for three InP (110) surfaces with different carrier concentrations: The *solid lines* should guide the eye. **b** Relative changes of the barrier height for the formation of positively charged P vacancies on p-doped InP (110) surfaces as a function of the position of the Fermi energy of the surface. *Filled triangles* show the data for surface Fermi level positions equal to those in the bulk and *open triangles* show data for Fermi level positions determined by the bulk and by the vacancy-induced surface band bending. Adapted with permission from [58]. ©2001 American Institute of Physics

have to address what physical quantities govern the initial formation of the vacancies. In the case of *thermal equilibrium* or in the case of infinite time after cleavage, the vacancies observed on the surface can reach their equilibrium concentration. The equilibrium concentrations are controlled by the vacancy *formation energy*, which is the difference in free enthalpy between the initial state with no vacancy in the surface and the final state with a vacancy in the surface and the missing atom moved to a reservoir. These quantities are those calculated in Fig. 4. The *kinetic* increase of the vacancy concentration is, however, governed by the *energy barrier* for the formation of the vacancy. Thus we first have to consider the different kinetic processes which affect the concentration of surface vacancies. Our model is a Langmuir evaporation of phosphorus via two successive steps, vacancy formation and desorption of P_2 molecules/clusters [38]. On this basis the formation of vacancies can be described with simple rate equations taking three processes into account: the formation of vacancy–adatom pairs, the recombination of an adatom with a vacancy, and the formation of P_2 molecules followed by immediate evaporation. The change of the vacancy concentration c_V with time t is thus

$$\mathrm{d}c_V/\mathrm{d}t = \upsilon \cdot \mathrm{e}^{-\frac{B}{kT}} \cdot (1 - Zc_V) - K_{AV}c_A c_V \quad . \tag{3}$$

The corresponding equation for the change of the adatom concentration c_A with time is

$$\mathrm{d}c_A/\mathrm{d}t = \mathrm{d}c_V/\mathrm{d}t - K_{AA}c_A^2 \tag{4}$$

where υ is an attempt frequency and B the activation or energy *barrier* for the formation of vacancy–adatom pairs. k denotes the Boltzmann constant. K_{AV} and K_{AA} are the rate coefficients for the vacancy–adatom recombination process and the formation of the P_2 molecule, respectively, including its subsequent desorption. Z is the number of sites around each vacancy in which no other vacancy can be created, e.g. due to charge repulsion. Note that Eqs. (3) and (4) cannot explain without further assumptions the decrease of the vacancy-formation rates above 435 K. This decrease is due to an effective P vacancy diffusion into the bulk starting at higher temperatures [51]. We therefore limit our further analysis for the determination of the barrier B to the room-temperature measurements in Fig. 8a, where indiffusion is negligible. Furthermore at room temperature only a few vacancies are formed because the kinetics are slow and the low concentration limit reduces the number of adatoms to such a degree that the adatom–vacancy recombination part can be neglected. For short annealing times and low vacancy concentrations Eq. (3) can thus be simplified to

$$\left.\frac{\mathrm{d}c_V}{\mathrm{d}t}\right|_{t\to 0} = \upsilon \cdot \mathrm{e}^{-\frac{B}{kT}} \quad . \tag{5}$$

Note that this approximation assumes as a rate-limiting process the formation of the adatom, which leaves a vacancy behind. This assumption is corroborated by (i) the observation of vacancy-denuded zones along steps, implying that steps are not the source of vacancies and (ii) the very low concentration (if any) of adatoms, suggesting an immediate evaporation of P_2.

Equation (5) describes an apparently linear dependence of the vacancy concentration as a function of time. This is, however, not the case, since the barrier B is not constant, but rather a function of the position of the Fermi energy as demonstrated below (the Fermi level at the surface in turn is shifted by small concentrations of positively charged surface vacancies, see Fig. 5).

For the determination of the barrier height B the attempt frequency can be approximated by the Debye frequency (8.8 THz) [64] or by the phonon frequencies of the InP (110) surface (2–10 THz) [65, 66]. The barrier can then be deduced from the slope of the data ($\mathrm{d}c/\mathrm{d}t$) at infinitely small vacancy concentration ($t \to 0$). For the highest-doped sample we found a barrier height B of 1.19 ± 0.05 eV [58]. This barrier is much smaller than those calculated by Yi et al. [67] (5.4 eV for V_{As} on GaAs (110)), Ong et al. [68] (2.73 eV for V_{Ga} on GaP (110)), and Itoh et al. [69] (2.82 eV for V_P on GaP (110)). The measured barrier height scales rather with diffusion barriers of As vacancies on GaAs (110) surfaces of 1.3 and 1.5 eV [70, 71].

At this stage we address the effect of the carrier concentration. This is simplified when analyzing the relative changes of the barrier (not affected by the attempt frequency) as a function of the position of the Fermi energy at the surface. Figure 8b shows the relative variations of the barrier height as a function of the position of the Fermi energy on the surface [58]. Three data points (filled squares) were extracted from the data extrapolated to the cleavage time (Fermi energy on the surface equals that in the bulk) and three data points (open circles) were determined for vacancy concentrations of about 0.1 to 0.15%. In the latter case the vacancies induced already a band bending at the surface calculated according to Eqs. (1) and (2). The error bars given indicate the relative temperature uncertainty and the error of the determination of the slope. All data points suggest a linear dependence of the barrier height for vacancy formation on the position of the Fermi energy on the surface [72]. The excellent agreement of the data points shown as open circles (values *with* surface band bending) with those shown as filled squares (*no* band bending at the surface), shows that the barrier is only affected by the position of the Fermi energy at the *surface* and not by that in the bulk crystal. The data also suggests that the formation of the vacancies is driven by the Fermi-level effect [73, 74].

1.5 Interactions of vacancies

The electrical charge of the vacancies leads to charge-induced interactions of the vacancies with both other vacancies and dopant atoms. Interactions between vacancies are repulsive and are governed by the screened Coulomb potential at the surface. We measured the potential for P vacancies using the statistical distribution of vacancies after prolonged annealing [50] and found for all temperatures the same potential, something true only in equilibrium conditions. The potential obtained can be well described by a screened Coulomb potential with a surface screening length much smaller than that in the bulk. The origin of the short screening length is unclear as little is known about surface screening itself.

Interactions with dopant atoms give rise to defect complexes in the surface. Since the physics governing these interactions is similar to that found for the compensation mechanisms of bulk dopant atoms, we briefly introduce the sur-

face analogue here. A freshly cleaved p-doped InP (110) surface typically exhibits very few defects. When annealed the concentration of P vacancies increases [38]. With increasing P vacancy concentration, the probability of finding a close P-vacancy–Zn-dopant pair grows and new types of defect such as those shown in Fig. 9a and b can be observed [51]. These defects are not surrounded by any height changes (elevation or depression) like those around charged dopant atoms and charged vacancies (see also Fig. 1). Thus, they do not induce band bending and are uncharged. They always consist of one localized hole of the size of one P dangling bond and one or two apparently raised neighboring dangling bonds. Figure 9c and d show P vacancies at different distances from Zn-dopant atoms. Zn-vacancy pairs with a large separation do not affect each other's appearance and properties. However, as the separation is reduced, both the P vacancy and the Zn-dopant atom have a less pronounced local band bending (compare the two dopant atoms in Fig. 9c), because the depletion zone around the P vacancy is compensated by the accumulation zone around the charged Zn-dopant atom [43, 51]. With decreasing separation the band bending eventually disappears and the complexes are uncharged. Close inspection of the voltage dependence shows, however, that there is still a small charge accumulation and depletion at the site of the Zn-dopant atom and the P vacancy, respectively [51] and thus the vacancy–dopant atom complexes are atomic scale dipoles surrounded by a dipole screening field. From the overall charge neutrality once can conclude that the vacancy and the dopant atom have the same magnitude of charge only with opposite polarity [43, 51]. If one assumes that a near-surface Zn-dopant atom has a charge of $-1e$ as in the bulk the P vacancy must have a $+1e$ charge. Note that the formation of vacancy–dopant complexes is driven by an attractive Coulomb interaction arising from the opposite charges of the P vacancies and the Zn-dopant atoms [51]. Analogous effects were found for As vacancies and Zn-dopant atoms in p-doped GaAs(110) surfaces [43, 48, 49] as well as for bulk As vacancy–Si donor [47] and Ga vacancy–Si donor complexes [57, 75] exposed on n-doped GaAs (110) cleavage surfaces.

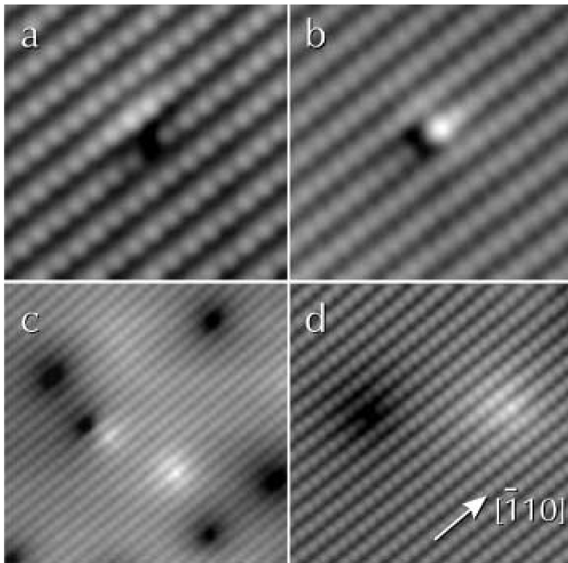

Fig. 9a–d. Interaction of P vacancies with Zn dopant atoms in the p-doped InP (110) surfaces. **a** and **b** show two P-vacancy-Zn-dopant complexes with a different relative arrangement of the P vacancy and the Zn-dopant atom, whereas **c** and **d** show P vacancies an Zn-dopant atoms forming dipoles with different separations. Adapted with permission from [51]. ©1996 American Physical Society

2 Investigation of bulk point defects and dopant atoms

Perhaps the prototype bulk point-like 'defects' are impurities, notably dopant atoms. Due to their outstanding technological importance, their atomically resolved imaging such as that shown in Fig. 1 attracted wide interest. The first identification of dopant atoms in cross-sectional STM images was published by Feenstra et al. [76] for Si dopants in GaAs multilayer structures and by Ebert and Urban for Zn-dopant atoms in GaP [28]. This was rapidly followed by a detailed characterization of Si [57, 77–80], Zn [81, 82], and Be [83–85] dopants in GaAs, Zn-dopant atoms [51] in InP, as well as S in InAs [24, 86] (110) surfaces. Indium-dopant atoms were also identified in cleavage surfaces of wurtzite-structure CdSe and CdS [87]. With a few exceptions these works concentrate on the pure imaging and identification of dopant atoms in the surface and subsurface layers on the basis of the contrast and symmetry of the screening clouds surrounding the charged dopants. Here we are interested in extracting the physics governing dopant atoms, notably their interactions and compensation. We first address the screened Coulomb interaction between Zn-dopant atoms in GaAs and then the methodology to identify the defects compensating Si donors in GaAs. Both problems are related to each other by the fact that the same physics is involved and by the fact that a purely bulk case is investigated by a surface-sensitive method.

2.1 Screening of charged impurities in the bulk: the screened Coulomb potential

Every charged defect or dopant induces a local variation of the electrostatic potential. The extent of this potential governs the interaction range of a charged defect with other charged defects, whereas the magnitude of the potential is a hint for the strength of the interaction. Inside a semiconductor the magnitude as well as the extent of the initial Coulomb potential is reduced by a redistribution of the free charge carriers. For example, a positively charged defect attracts electrons in the conduction band and repels holes in the valence band. The negative charge of the excess electrons and/or of the missing holes (screening cloud) smoothes or screens the original Coulomb potential of the positively charged defect. The potential modified by the presence of screening charge carriers becomes a *screened Coulomb potential*:

$$V(r) = \frac{e}{4\pi\varepsilon_0\varepsilon_r r} \cdot \mathrm{e}^{-\frac{r}{R_\mathrm{S}}} \tag{6}$$

with R_S being the screening length (here screening by holes in the valence band) [88]:

$$R_\mathrm{S} = \sqrt{\frac{2\pi^2\varepsilon_0\varepsilon_r\hbar^3}{e^2 m_\mathrm{h}{}^{3/2}(2\pi kT)^{1/2} \cdot \mathrm{F}_{-1/2}(\eta)}} \tag{7}$$

m_h is the effective mass of the holes. $F_l(\eta)$ are the Fermi–Dirac integrals with the reduced Fermi energy $\eta = E_F/kT$. At small distances it becomes identical with the unscreened Coulomb potential, whereas at large distances it decays much faster. The extent is governed by the screening length. The key parameter in the screened Coulomb potential is the screening length given in Eq. (7). For several decades this parameter could not be measured and one had to rely on the theoretical model only.

Here we illustrate how to measure directly the screening length by cross-sectional scanning tunneling microscopy [89]. We extracted the positions of all dopant atoms exposed on a GaAs (110) cleavage surface from the STM images and analyzed their spatial distribution to extract their mutual interactions. Since all the dopant atoms are negatively charged, they mutually interact with the repulsive screened Coulomb potential. The repulsive interaction can be quantified by deducing from the STM images the positions of all the dopant atoms and by calculating the distances r between all possible pairs of dopants [50, 90]. This yields the pair correlation function $c(r)$ of the dopant atoms, which is related to the so-called 'mean force potential', $W(r)$, through [91]

$$W(r) = -kT \cdot \ln[c(r)] \ . \quad (8)$$

Although it is in principle possible to distinguish dopant atoms in different subsurface layers, in practical cases the need to achieve sufficient statistics requires large-scale images, where the subsurface-layer determination of a dopant (based on the symmetry in high-resolution STM images) is not possible any more. Therefore we used in Eq. (8) for r the dopant–dopant separation projected on the surface. This projected 'view' is properly taken into account and does not affect the results, because the respective simulation is performed in an analogous manner as discussed below. Furthermore, it should be noted that only if the extent of the interaction is smaller than the average separation of the dopants (low-density limit), correlation effects can be neglected and the mean force potential equals the interaction energy [91]. In the specific case of the dopant atoms this approximation turned out to be not valid due to strong many-body effects in the dopant interactions leading to a clustering of dopant atoms [89]. Nevertheless it is possible to extract the intrinsic screening length by a two-step process. First we fit the values $-\ln[c(r)]$ with a Yukawa potential to determine the *apparent* screening length as a function of the carrier concentration (filled squares in Fig. 10). As expected, the apparent screening length increases with decreasing carrier concentration. However, the data do not agree quantitatively with the theoretical values for the intrinsic screening length (solid line in Fig. 10) determined according to Eq. (7) for a freeze-in temperature of 900 K, because of the importance of many-body effects in the otherwise repulsive interaction between the dopants [89]: indeed for a collection of mutually repulsive particles, strong many-body effects can lead to a shorter apparent screening length than the true one. We have proven this for the present system by performing Monte Carlo simulations of the experiment [89]. In the simulation dopant atoms surrounded by the screened Coulomb potential were positioned in a model crystal and allowed to arrange their spatial positions. After reaching the equilibrium configuration we analyzed the spatial distribution of the dopant atoms exactly as we did for the STM images to determine the (output) screening length from the simulated pair correlation function as a function of the (input) screening lengths of the Yukawa potential. At the experimental dopant concentrations the output screening lengths are considerably smaller than the input screening lengths due to many-body effects, i.e. interactions between more than two dopant atoms. Using these simulations we determined the intrinsic screening length in the GaAs crystals as a function of the carrier concentration by comparing the measured apparent screening length with the output screening length of the simulation. The corresponding input screening length is the intrinsic one. The input screening lengths (empty squares in Fig. 10) agree very well with the theoretical calculations according to (7) at 900 K (solid line in Fig. 10). Thus the local screened potential around charged impurities and defects in GaAs is well described by Eqs. (6) and (7). Note that so far no other experiment allowed us to extract the intrinsic screening length in semiconductors and cross-sectional STM is the only access to such microscopic data.

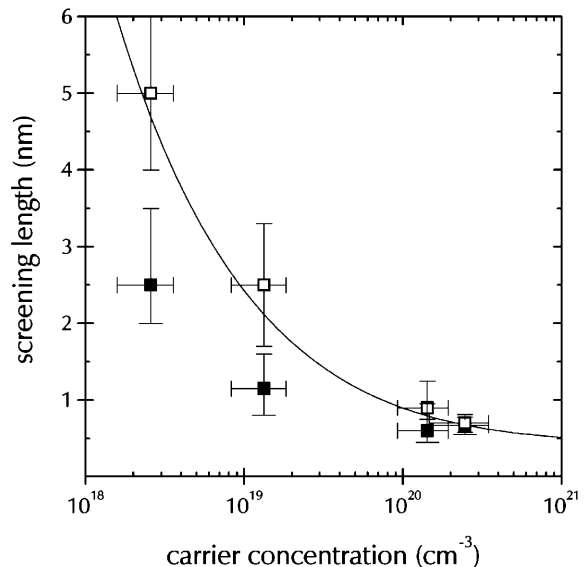

Fig. 10. Measured values for screening lengths R_S as a function of the carrier concentration (*filled squares*). The *solid line* represents the theoretical screening length calculated according to (7) for 900 K. The *open squares* show the screening length corrected for many-body interactions. Reprinted with permission from [51]. ©1999 American Physical Society

2.2 *Compensation of* Si *donors in as-grown highly* Si*-doped* GaAs

The extent to which *microscopic* data and the physics governing bulk defects can be obtained from STM images has been demonstrated perhaps most impressively by Domke et al. [47, 57] using the example of Si-doped GaAs. Here we illustrate the methodology and provide an outlook of to what degree such atomic scale data can be used to advance the physics and calibrate for example positron annihilation.

We used four steps to determine the types and concentrations of defects in the bulk from high-resolution STM images [57]. First, we identified all defects occurring on (110) cleavage planes of the GaAs crystals. Secondly, we measure,

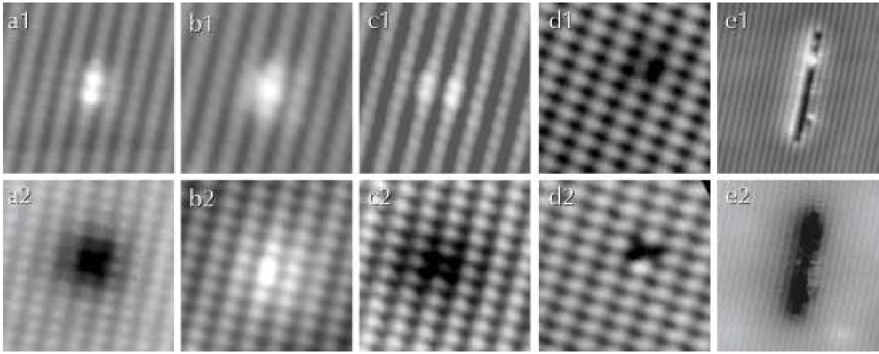

Fig. 11a–e. Images of occupied (upper frames) and empty (lower frames) density of states of the major defects on Si-doped GaAs(110) surfaces. **a1** and **a2** show a Ga vacancy, **b1** and **b2** a Si_{Ga} donor, **c1** and **c2** a Si_{As} acceptor, **d1** and **d2** a Si_{Ga}-Ga-vacancy complex, and **e1** and **e2** the intersection line of a planar Si cluster. The tunneling voltages are **a1** -2.4 V, **a2** $+1.8$ V, **b1** -2.0 V, **b2** $+1.4$ V, **c1** -2.0 V, **c2** $+1.4$ V, **d1** -2.0 V, **d2** $+1.4$ V, **e1** -2.2 V, and **e2** $+1.5$ V. The defects were observed on cleavage planes of as-grown bulk crystals. Adapted with permission from [57]. ©1996 American Physical Society

by counting individual defects in the STM images, the concentrations per surface and/or subsurface layer separately for all defects. Thirdly, we separate all surface defects formed after cleavage from *bulk* defects exposed by cleavage on the surface by analyzing the time dependence of the defect concentrations. In the fourth step we calculate the bulk concentrations of each defect from the measured concentrations per layer. The last step provides the desired microscopic information on the types and concentrations of the defects present inside the crystal [57].

The four procedures have been applied [57] to three as-grown GaAs crystals with different Si concentrations chosen such that they cover a large Si concentration range ranging from 2.7×10^{18} to $(2.5-6) \times 10^{19}\,\mathrm{cm}^{-3}$. Simultaneously the fraction of electrically inactive Si-dopant atoms increased from 55 to 95%. The STM images revealed a strong increase of the concentration of various defects with increasing Si-doping concentration of the crystals [57]. All defects observed were identified on the basis of simultaneously measured, high-resolution STM images of the occupied (Fig. 11 a1–e1) and empty states (Fig. 11 a2–e2). Five major defects were observed in all samples with varying concentration [57]. These are surface gallium vacancies (V_{Ga}) (Fig. 11 a1 and a2) formed after cleavage and thus not of interest below, Si_{Ga} donors (frames (b1) and (b2) of Fig. 11) as well as Si_{As} acceptors ((c1) and (c2)), Si donor-Ga vacancy complexes (Si_{Ga}–V_{Ga}) shown in frames (d1) and (d2) of Fig. 11, and Si clusters cut by the cleavage plane (Fig. 11 e).

We now measured the near-surface concentrations of all these defects and dopant atoms. In the absence of any diffusion at room temperature the surface concentrations reflect the bulk concentrations. The *bulk* concentrations of Si incorporated in the defects determined from the STM images are summarized in Fig. 12 as a function of the total Si-dopant concentration incorporated into the crystals during growth (measured by SIMS (secondary ion mass spectroscopy)) [57]. The sum of the STM-based Si concentrations in all defects agrees well with the expected total concentration of Si measured by SIMS, indicating that the Si-containing defects were correctly identified. The data reveals three trends: a nearly constant concentration of Si donors, a consecutive onset of three compensation mechanisms at specific critical Si concentrations, and the large majority of Si not being incorporated as donors [57].

At this stage we focus on the identification of the physics governing the compensation of Si donors. In contrast to the data shown in Fig. 12, calculations expect a strong increase of the concentration of donors and acceptors with the Si doping [92]. Since this is not observed, we proposed an explanation based on a screened-Coulomb-interaction-limited solubility of Si in GaAs [57]: Si is initially incorporated only on Ga sites as donors. If Si behaved like an ideal donor, the carrier concentration would closely follow the concentration of Si and the screening of the charged Si dopants would become more and more effective (see Fig. 10). However, with increasing n-type doping the formation energy of Si_{As} acceptors decreases [93] and Si is increasingly incorporated on As sites as acceptors [94] (see also Fig. 12). Thus, the carrier concentration and the efficiency of the screening are reduced. Consequently Coulomb interactions become rele-

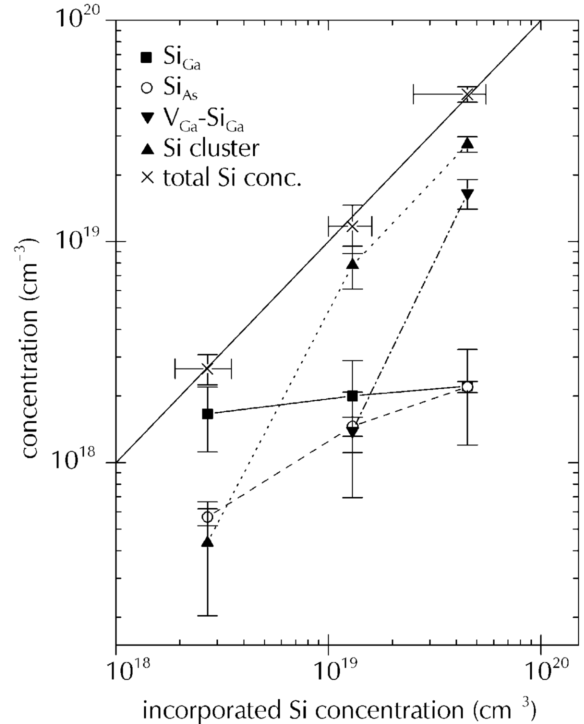

Fig. 12. Si concentration present in Si_{Ga} donors (■), Si_{As} acceptors (○), Si clusters (▲), and $V_{Ga}-Si_{Ga}$ complexes (▼) as a function of the Si doping concentration incorporated into the crystals during growth. The Si doping concentration incorporated during growth has been measured by secondary ion mass spectroscopy (SIMS). The sum of the Si concentrations of the different defects measured in the STM images (×) agrees well with the measured by SIMS (*solid line*). The *horizontal error bars* originate from the SIMS measurements. They should be applied to all the respective data points. All *vertical error bars* show the reproducibility of the STM measurements. Adapted with permission from [57]. ©1996 American Physical Society

vant between the increasing number of positively charged Si_{Ga} donors and negatively charged Si_{As} acceptors and uncharged Si pairs are formed. Thus the screened Coulomb interaction is the driving force for the Si pair and cluster formation and therefore also governs the solubility limit of Si in GaAs [57]. Consequently, the density of charged Si donors and acceptors remains essentially constant although the Si concentration increases by more than one order of magnitude, because the carrier concentration does not change much. This model explains the observation of a nearly constant donor and acceptor concentration, in contrast to theoretical predictions, which did not take interactions into account.

The decrease of the charge-carrier concentration at very high Si-doping concentration can be explained by the formation of (Si_{Ga}–V_{Ga}) complexes [57]. The Ga vacancy formation energy is lowered with increasing n-type doping [92, 93], due to the Fermi-level effect [74]. Thus, negatively charged Ga vacancies are formed, which attract positively charged Si donors and vacancy–donor complexes are formed [51]. The formation of complexes is a mechanism analogous to that driving the Si pair formation.

This example demonstrates that the scanning tunneling microscope can be used successfully to identify the concentrations and the types of bulk defects present in III–V semiconductors. These microscopic data provide an invaluable basis for the determination of the physics governing the defects and of the mechanisms taking place inside the crystals. The examples investigated so far demonstrate that such measurements may also serve as the basis for testing present theoretical concepts of the physics governing point defects and thus initiate significant advances in the understanding of the properties of novel electronic materials. Furthermore, we used such microscopic data to calibrate positron-annihilation signals and relate them to individual defects [75, 95]. Such a calibration of other methods is particularly promising for practical applications. Although STM provides the most detailed microscopic defect information and the best basis for a determination of the physics governing point defects, in practical uses, however, the integrating methods, such as positron annihilation, can be applied routinely, while the STM, due to its complexity and time requirement, remains a method which can only be applied to specific well-chosen examples.

3 Summary

We illustrated the possibilities to obtain nano-scale physical properties of individual point defects and dopant atoms exposed in and below cleavage surfaces of compound semiconductors – primarily by cross-sectional scanning tunneling microscopy (STM). Using the example of the phosphorus *surface* vacancy in InP(110) surfaces, we demonstrated that the existence of localized defect states, the electrical charge state, the static and non-static atomic structure, the defect-formation barrier, and the interactions between different defects and/or dopant atoms, can be determined quantitatively. The knowledge about surface defects eventually culminates in the possibility of addressing point defects and dopant atoms in the bulk. We demonstrated this possibility, on the one hand, by measuring for the first time the screening length in GaAs microscopically and, on the other hand, by determining directly the types and concentrations of defects compensating Si donors inside GaAs crystals. We achieved the identification of the physical processes governing the bulk defects and dopant atoms and highlighted the importance of the interactions mediated by the screened Coulomb potential. So far STM is the only technique providing such microscopic data, which is an excellent basis for the determination of the physics of defects and the mechanisms taking place inside the crystals.

Acknowledgements. I would like to thank S. Blügel, C. Domke, J. Gebauer, M. Heinrich, K. Horn, F. Kluge, M.G. Lagally, J. Neugebauer, M. Scheffler, G. Schwarz, U. Semmler, C.K. Shih, K. Urban, M.B. Webb, T. Zhang, and Zhenyu Zhang for very enjoyable and successful collaborations and K.H. Graf for excellent technical support.

References

1. Ph. Ebert: Surf. Sci. Rep. **33**, 121 (1999)
2. D.J. Chadi: Phys. Rev. B **19**, 2074 (1979)
3. D.J. Chadi: Phys. Rev. Lett. **41**, 1062 (1978)
4. C.B. Duke: *Reconstruction of the Cleavage Faces of Tetrahedrally Coordinated Compound Semiconductors*. In: Festkörperprobleme, Advances in Solid State Physics, Vol. 33, ed. by R. Helbig (Vieweg, Braunschweig, Wiesbaden 1994) pp. 1–36
5. R. Chang, W.A. Goddard, III: Surf. Sci. **144**, 311 (1984)
6. A. Kahn: Surf. Sci. Rep. **3**, 193 (1983)
7. D.H. Lee, J.D. Joannopoulos: J. Vac. Sci. Technol. **21**, 351 (1982)
8. M. Sabisch, P. Krüger, J. Pollmann: Phys. Rev. B 51, 13 367 (1995)
9. A.R. Lubinsky, C.B. Duke, B.W. Lee, P. Mark: Phys. Rev. Lett. **36**, 1058 (1976)
10. J.R. Chelikowsky, M.L. Cohen: Phys. Rev. B **20**, 4150 (1979)
11. D.V. Froelich, M.E. Lapeyre, J.D. Dow, R.E. Allen: Superlattices Microstruct. **1**, 87 (1985)
12. R.M. Feenstra, J.A. Stroscio, J. Tersoff, A.P. Fein: Phys. Rev. Lett. **58**, 1192 (1987)
13. W. Mönch: Work Function and Bending at Semiconductor Surfaces, ed. by R. Vanselow, R. Howe (Springer Ser. Chem. Phys. Phys. Solid Surf. V 35) (Springer, Berlin, Heidelberg, New York 1984) pp. 501–534
14. W. Mönch: Semiconductor Surfaces and Interfaces, ed. by G. Ertl, R. Gomer, D.L. Mills (Springer Ser. Surf. Sci. 26) (Springer, Berlin, Heidelberg, New York 1993)
15. A. Huijser, J. van Laar, T.L. van Rooy: Surf. Sci. **62**, 472 (1977)
16. A. Huijser, J. van Laar, T.L. van Rooy: Phys. Lett. 65A, 337 (1978)
17. L. Sorba, V. Hinkel, H.U. Middelmann, K. Horn: Phys. Rev. B **36**, 8075 (1987)
18. B. Reihl, T. Riesterer, M. Tschudy, P. Perfetti: Phys. Rev. B 38, 13 456 (1988)
19. H. Carstensen, R. Claessen, R. Manzke, M. Skibowski: Phys. Rev. B **41**, 9880 (1990)
20. Ph. Ebert, B. Engels, P. Richard, K. Schroeder, S. Blügel, C. Domke, M. Heinrich, K. Urban: Phys. Rev. Lett. **77**, 2997 (1996)
21. G. Cox, Ph. Ebert, K. Urban: Inst. Phys. Conf. Ser. **117**, 347 (1991)
22. G. Lengel, R. Wilkins, G. Brown, M. Weimer: J. Vac. Sci. Technol. B **11**, 1472 (1993)
23. G. Lengel, R. Wilkins, G. Brown, M. Weimer, J. Gryko, R.E. Allen: Phys. Rev. Lett. **72**, 836 (1994)
24. A. Depuydt, N.S. Maslova, V.I. Panov, V.V. Rakov, S.V. Savinov, C. Van Haesendonck: Appl. Phys. A 66, S171 (1998)
25. Ph. Ebert, G. Cox, U. Poppe, K. Urban: Ultramicroscopy **42–44**, 871 (1992)
26. Ph. Ebert, K. Urban, M.G. Lagally: Phys. Rev. Lett. **72**, 840 (1994)
27. M. Heinrich, Ph. Ebert, M. Simon, K. Urban, M.G. Lagally: J. Vac. Sci. Technol. A **13**, 1714 (1995)
28. Ph. Ebert, K. Urban: Ultramicroscopy **49**, 344 (1993)
29. L.J. Whitman, J.A. Stroscio, R.A. Dragoset, R.J. Celotta: Phys. Rev. B **42**, 7288 (1990)
30. L.J. Whitman, J.A. Stroscio, R.A. Dragoset, R.J. Celotta: J. Vac. Sci. Technol. B **9**, 770 (1991)
31. G. Cox, K.H. Graf, D. Szynka, U. Poppe, K. Urban: Vacuum **41**, 591 (1990)

32. G. Lengel, R. Wilkins, M. Weimer, J. Gryko, R.E. Allen: In: Proceedings of the 22nd International Conference on the Physics of Semiconductors, Vancouver, BC, Canada, 15–19 August 1994, Vol. 1, ed. by D.J. Lockwood (World Scientific, Singapore 1995) p. 479
33. Ph. Ebert, K. Urban: Phys. Rev. B **58**, 1401 (1998)
34. B. Siemens, C. Domke, Ph. Ebert, K. Urban: Thin Solid Films **343–344**, 531 (1999)
35. S.B. Zhang, A. Zunger: Phys. Rev. Lett. **77**, 119 (1996)
36. H. Kim, J.R. Chelikowsky: Phys. Rev. Lett. **77**, 1063 (1996)
37. G. Schwarz, A. Kley, J. Neugebauer, M. Scheffler: Phys. Rev. B **58**, 1392 (1998)
38. Ph. Ebert, M. Heinrich, M. Simon, K. Urban, M.G. Lagally: Phys. Rev. B **51**, 9696 (1995)
39. Ph. Ebert, K. Urban, L. Aballe, C.H. Chen, K. Horn, G. Schwarz, J. Neugebauer, M. Scheffler: Phys. Rev. Lett. **84**, 5816 (2000)
40. R.J. Hamers: J. Vac. Sci. Technol. B **6**, 1462 (1988)
41. J.A. Stroscio, R.M. Feenstra, A.P. Fein: Phys. Rev. Lett. **58**, 1668 (1987)
42. C. Domke, M. Heinrich, Ph. Ebert, K. Urban: J. Vac. Sci. Technol. B **16**, 2825 (1998)
43. K.J. Chao, A.R. Smith, C.K. Shih: Phys. Rev. B **53**, 6935 (1996)
44. G. Schwarz: Untersuchung von Defekten auf und nahe der (110) Oberfläche von GaAs und weiteren III–V Halbleitern. Thesis, Technische Universität Berlin, in preparation
45. H. Kim, J.R. Chelikowsky: Surf. Sci. **409**, 435 (1998)
46. G. Schwarz: Theoretische Untersuchungen zu Leerstellen auf der (110)-Oberfläche von GaP. Diplomarbeit, Technische Universität Berlin (1996)
47. C. Domke, Ph. Ebert, K. Urban: Phys. Rev. B **57**, 4482 (1998)
48. K.-J. Chao, A.R. Smith, C.K. Shih: J. Vac. Sci. Technol. B **14**, 948 (1996)
49. Ph. Ebert, M. Heinrich, K. Urban, K.-J. Chao, A.R. Smith, C.K. Shih: J. Vac. Sci. Technol. A **14**, 1807 (1996)
50. Ph. Ebert, Xun Chen, M. Heinrich, M. Simon, K. Urban, M.G. Lagally: Phys. Rev. Lett. **76**, 2089 (1996)
51. Ph. Ebert, M. Heinrich, M. Simon, C. Domke, K. Urban, C.K. Shih, M.B. Webb, M.G. Lagally: Phys. Rev. B **53**, 4580 (1996)
52. S. Aloni, I. Nevo, G. Haase: Phys. Rev. B **60**, R2165 (1999)
53. J. Harper, G. Lengel, R.E. Allen, M. Weimer: Phys. Rev. Lett. **79**, 3312 (1997) ; (Erratum) Phys. Rev. Lett. **80**, 643 (1998)
54. J. Harper, G. Lengel, R.E. Allen, M. Weimer: Phys. Rev. Lett. **79**, 3314 (1997)
55. J. Dabrowski, M. Scheffler: Appl. Surf. Sci. **56–58**, 15 (1990)
56. K. Hata, Y. Sainoo, H. Shigekawa: Phys. Rev. Lett. **86**, 3084 (2001)
57. C. Domke, Ph. Ebert, M. Heinrich, K. Urban: Phys. Rev. B 54, 10 288 (1996)
58. U. Semmler, M. Simon, Ph. Ebert, K. Urban: J. Chem. Phys. **114**, 445 (2001)
59. R.F.C. Farrow: J. Phys. D: Appl. Phys. **7**, 2436 (1974)
60. W.Y. Lum, A.R. Clawson: J. Appl. Phys. **50**, 5296 (1979)
61. P.K. Gallagher, S.N.G. Chu: J. Phys. Chem. **86**, 3246 (1982)
62. L.G. Van Uitert, P.K. Gallagher, S. Singh, G.J. Zydzik: J. Vac. Sci. Technol. B **1**, 825 (1983)
63. Ph. Ebert, M.G. Lagally, K. Urban: Phys. Rev. Lett. **70**, 1437 (1993)
64. J.C. Brice: in Properties of Indium Phosphide (INSPEC 1991) p. 18
65. H. Nienhaus, W. Mönch: Surf. Sci. Lett. **328**, L561 (1995)
66. U. Schroeder, J. Fritsch, P. Pavone: Physica B **219–220**, 434 (1996)
67. J.-Y. Yi, J.S. Ha, S.-J. Park, E.-H. Lee: Phys. Rev. B **51**, 11 198 (1995)
68. C.K. Ong, G.S. Khoo, K. Hattori, Y. Nakai, N. Itoh: Surf. Sci. Lett. **259**, L787 (1991)
69. N. Itoh, K. Hattori, Y. Nakai, J. Kanasaki, A. Okano, C.K. Ong, G.S. Khoo: Appl. Phys. Lett. **60**, 3271 (1992)
70. R.J. Pechman, X.-S. Wang, J.H. Weaver: Phys. Rev. B **51**, 10 929 (1995)
71. G. Lengel, M. Weimer, J. Gryko, R.E. Allen: J. Vac. Sci. Technol. A **12**, 1855 (1994)
72. U. Semmler, Ph. Ebert, K. Urban: Appl. Phys. Lett. **77**, 61 (2000)
73. T.Y. Tan, U. Gösele, S. Yu: Crit. Rev. Solid State Mater. Sci. **17**, 47 (1991)
74. T.Y. Tan, H.-M. You, U.M. Gösele: Appl. Phys. A **56**, 249 (1993)
75. J. Gebauer, R. Krause-Rehberg, C. Domke, Ph. Ebert, K. Urban: Phys. Rev. Lett. **78**, 3334 (1997)
76. R.M. Feenstra, E.T. Yu, J.M. Woodall, P.D. Kirchner, C.L. Lin, G.D. Pettit: Appl. Phys. Lett. **61**, 795 (1992)
77. J.F. Zheng, X. Liu, N. Newman, E.R. Weber, D.F. Ogletree, M. Salmeron: Phys. Rev. Lett. **72**, 1490 (1994)
78. J.F. Zheng, X. Liu, E.R. Weber, D.F. Ogletree, M. Salmeron: J. Vac. Sci. Technol. A **12**, 2104 (1994)
79. M.C.M.M. van der Wielen, A.J.A. van Roij, H. van Kempen: Phys. Rev. Lett. **76**, 1075 (1996)
80. B. Grandidier, J.P. Nys, X. Wallart, D. Stiévenard: Appl. Phys. Lett. **72**, 2454 (1998)
81. M. Simon, C. Dzeja, Ph. Ebert, H.-G. Hettwer, W. Jäger, A. Rucki, K. Urban: In: Formation of Semiconductor Interfaces, ICFSI-4, 14–18 June 1993, Forschungszentrum Jülich, Germany, ed. by B. Lengeler, H. Lüth, W. Mönch, J. Pollmann (World Scientific, Singapore 1994) p. 49
82. J.F. Zheng, M. Salmeron, E.R. Weber: Appl. Phys. Lett. **64**, 1836 (1994)
83. M.B. Johnson, O. Albrektsen, R.M. Feenstra, H.W.M. Salemink: Appl. Phys. Lett. **63**, 2923 (1993); (Erratum) Appl. Phys. Lett **64**, 1454 (1994)
84. M.B. Johnson, H.P. Meier, H.W.M. Salemink: Appl. Phys. Lett. **63**, 3636 (1993)
85. M.B. Johnson, P.M. Koenraad, W.C. van der Vleuten, H.W.M. Salemink, J.H. Wolter: Phys. Rev. Lett. **75**, 1606 (1995)
86. S. Gwo, S. Miwa, H. Ohno, J.-F. Fan, H. Tokumoto: Mater. Sci. Forum **196–201**, 1949 (1995)
87. B. Siemens, C. Domke, M. Heinrich, Ph. Ebert, K. Urban: Phys. Rev. B **59**, 2995 (1999)
88. R.B. Dingle: Philos. Mag. **46**, 831 (1955)
89. Ph. Ebert, T. Zhang, F. Kluge, M. Simon, Z. Zhang, K. Urban: Phys. Rev. Lett. **83**, 757 (1999)
90. K.-J. Chao, C.K. Shih, D.W. Gotthold, B.G. Streetman: Phys. Rev. Lett. **79**, 4822 (1997)
91. T.L. Hill: *Statistical Mechanics: Principles and Selected Applications* (McGraw-Hill Ser. Adv. Chem.) (McGraw-Hill, New York, Toronto, London 1956)
92. J.E. Northrup, S.B. Zhang: Phys. Rev. B **47**, 6791 (1993)
93. R.W. Jansen, O.F. Sankey: Phys. Rev. B **39**, 3192 (1989)
94. E.F. Schubert: *Doping in III–V Semiconductors* (Cambridge University Press, Cambridge, UK 1993)
95. J. Gebauer, R. Krause-Rehberg, C. Domke, Ph. Ebert, K. Urban, T.E.M. Staab: Phys. Rev. B **63**, 045203 (2001)